In situ Studies of Morphology Formation in Solution-Processed Polymer–Fullerene Blends

Esther Barrena, Felix Buss, Ana Perez-Rodriguez, Monamie Sanyal, Benjamin Schmidt-Hansberg, Michael F.G. Klein, Philip Scharfer, Wilhelm Schabel, and Uli Lemmer

Contents

1 Introduction 2
2 In situ Characterization of Film Formation During Drying 3
  2.1 Drying Channel and Experimental Setup 3
  2.2 Basics of Laser Reflectometry 4
  2.3 Experimental Details of the GIWAXS Measurements 6
3 Drying of P3HT/P_{61}CBM 7
  3.1 Binary Phase Diagram and Morphology Development 7
  3.2 Effect of the Blend Ratio 11
  3.3 Effect of the Drying Temperature 13
4 Drying of PSBTBT:PC_{71}BM 16
  4.1 In situ Study of the Crystallization of PSBTBT:PC_{71}BM 17
  4.2 Effect of the Drying Temperature 19
5 Conclusions 20
6 Acknowledgments 21
References 22

E. Barrena (✉) • A. Perez-Rodriguez
Instituto de Ciencia de Materiales de Barcelona (ICMAB CSIC), Campus UAB, Bellaterra, Barcelona 08193, Spain
e-mail: ebarrena@icmab.es

F. Buss • B. Schmidt-Hansberg • P. Scharfer • W. Schabel
Institute of Thermal Process Engineering, Thin Film Technology, Karlsruhe Institute of Technology, Kaiserstrasse 12, 76131 Karlsruhe, Germany
e-mail: wilhelm.schabel@kit.edu

M. Sanyal
Max Planck Institut für Metallforschung, Heisenbergstrasse 3, 70569 Stuttgart, Germany

M.F.G. Klein • U. Lemmer
Light Technology Institute, Karlsruhe Institute of Technology, Engesserstraße 13, 76131 Karlsruhe, Germany
e-mail: uli.lemmer@kit.edu

© Springer International Publishing Switzerland 2017

K. Leo (ed.), *Elementary Processes in Organic Photovoltaics*,
Advances in Polymer Science 272, DOI 10.1007/978-3-319-28338-8_1

Abstract Control of the blend nanomorphology in bulk heterojunctions (BHJs) is still a challenge that demands more fundamental knowledge of the mechanism of phase separation and crystallization during solvent drying. In this review we show that in situ studies using combined laser reflectometry and grazing-incidence wide-angle X-ray scattering provide a fundamental understanding on how the nanomorphology develops dynamically during film drying. We identify influencing parameters for controlled film formation in order to obtain optimized solar cell performance. We review here our results on BHJs of poly(3-hexylthiophene)–[6,6]-phenyl-C61-butyric acid methyl ester and poly{[4,40-bis(2-ethylhexyl)dithieno(3,2-b;20,30-d)silole]-2,6-diyl-alt-(2,1,3 benzothidiazole)-4,7-diyl} with [6,6]-phenyl-C71-butyric acid methyl ester.

Keywords Bulk heterojunction • Crystallization • Drying kinetics • GIWAXS • P3HT • PCBM • PSBTBT • Real-time studies • Solution processing

1 Introduction

Morphological control in bulk heterojunction (BHJ) photovoltaics is one pillar of the recent remarkable progress in the power conversion efficiency (PCE) of organic photovoltaic (OPV) devices [1–3]. The performance of solution-processed polymer solar cells is highly dependent on the phase-separated nanomorphology that dynamically forms during the drying process. Whether the polymeric component is in a crystalline or an amorphous state, pure or intermixed with the fullerene, with domain sizes on the order of magnitude of the exciton diffusion length or larger, are factors that largely affect the mechanisms involved in the energy-conversion process, that is, charges carrier photogeneration, dissociation, conduction, and collection.

In general, the final film structure that results upon solvent evaporation is not at thermodynamic equilibrium and, in addition, is very material dependent. The more quickly the drying step is performed, the less time remains for the solid components to arrange into their thermodynamically favored order. Consequently, quickly dried as-cast thin films fabricated into a functional OPV device generally exhibit a low PCE, requiring the use of an additional posttreatment step such as thermal annealing [4] or solvent annealing [5].

A more promising approach is to foster the formation of a more optimized nanomorphology in a solution, as recently exploited with the use of additives [1, 6]. However, predictive control of the blend nanomorphology remains a challenge that demands more fundamental knowledge of how the interplay between thermodynamic and kinetic factors (miscibility, solubility, blend ratio, solvent evaporation rate, etc.) triggers the evolution of the BHJ during film drying. To gain a full understanding of the mechanisms of phase separation and organization of the polymer and fullerene components, it is necessary to characterize the dynamic process of film formation from its earliest stage.

With this purpose, we designed a drying setup to monitor in real time the evolution of the thickness and structure in the wet film during solvent evaporation by combining laser reflectometry and grazing-incidence wide-angle X-ray scattering (GIWAXS). We performed extensive investigation of the blend system poly(3-hexylthiophene) (P3HT):[6,6]-phenyl-C61-butyric acid methyl ester (PCBM) and gained an understanding of the film structure formation [7, 8], the effect of the drying temperature [9], the role of PCBM [10], and the impact of using nonhalogenated solvent mixtures [11]. We also extended our studies to other material systems, such as poly{[4,40-bis(2-ethylhexyl)dithieno(3,2-b;20,30-d)silole]-2,6-diyl-alt-(2,1,3 benzothidiazole)-4,7-diyl} (PSBTBT) [11] and poly[2,6-(4,4-bis-(2-ethylhexyl)-4H-cyclopenta[2,1-*b*;3,4-*b*0]dithiophene)-*alt*-4,7(2,1,3-benzothiadiazole)] (PCPDTBT).

Here we review some of our results of the structural evolution during the drying of BHJ films of poly(3-hexylthiophene)–[6,6]-phenyl-C_{61}-butyric acid methyl ester (P3HT:PCBM) and poly{[4,40-bis(2-ethylhexyl)dithieno(3,2-*b*;20,30-d)silole]-2,6-diyl-*alt*-(2,1,3 benzothidiazole)-4,7-diyl}–[6,6]-phenyl-C_{71}-butyric acid methyl ester (PSBTBT:$PC_{71}BM$). We also provide detailed information on the experimental setup and the measurements performed in situ.

2 In situ Characterization of Film Formation During Drying

2.1 Drying Channel and Experimental Setup

Investigations of the drying behavior of polymer–fullerene films require a setup that facilitates the adjustment of all experimentally accessible drying parameters. In a drying channel the gas-phase drying conditions, that is, gas temperature T_g and velocity u_g, and the temperature of the substrate holder T_S, can be defined. An automated knife coater (doctor blade) allows the deposition of thin films in the range of several micrometers and subsequent drying. Immediately after coating, the drying process is monitored using two measurement techniques simultaneously: Laser reflectometry gives insight into the drying kinetics by providing information on the actual film thickness and composition, and simultaneously collected GIWAXS data reveal the appearance of structural features as the solid components begin to aggregate or crystallize. This setup enables the solubility limits and general thermodynamic properties that are known from supplementary measurements to be correlated to the onset and development of structure formation during the drying process (Fig. 1).

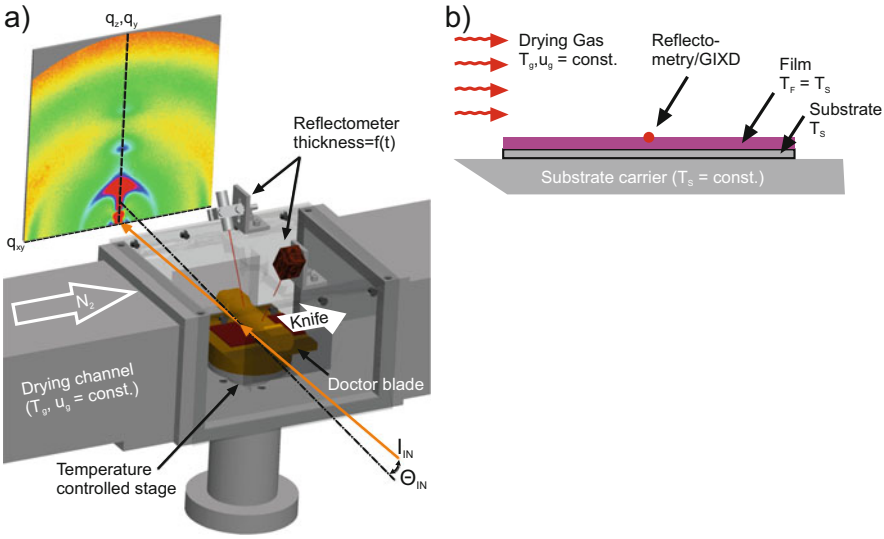

Fig. 1 Schematic of the experimental setup for simultaneous laser reflectometry and grazing-incidence wide-angle X-ray spectroscopy under controlled drying conditions [4]

2.2 Basics of Laser Reflectometry

Laser reflectometry is used in our experimental setup as a nondestructive method to determine the thickness of a transparent film [12–14]. In case of a drying film it is based on the optical interference of a laser beam that is reflected at the air–film and the film–substrate interfaces. As the film thickness decreases, constructive and destructive interference conditions of the reflected light are detected by a photodiode. With the knowledge of the refractive index and the dry film thickness, the thickness evolution over time can be calculated. Figure 2 illustrates the geometric conditions that need to be considered for the analysis of the reflectometry signal.

Using Snell's law of diffraction, basic geometric rules, and assuming a refractive index $n_0 = 1$ for the ambient, the difference in optical path [Eq. (1)] and the criterion for constructive and destructive interference [Eq. (2)] can be written as [8, 15]

$$\Delta = 2d\sqrt{n_1^2 - \sin^2\alpha} \tag{1}$$

$$\Delta = \frac{m}{2} \cdot \lambda, \tag{2}$$

where $m = [1, 2, 3, \ldots]$ with even (odd) values for constructive (destructive) interference and λ is the laser wavelength. Due to solvent evaporation, the refractive index n_1 of the solution is not a constant, but a function of the volume fractions φ_i

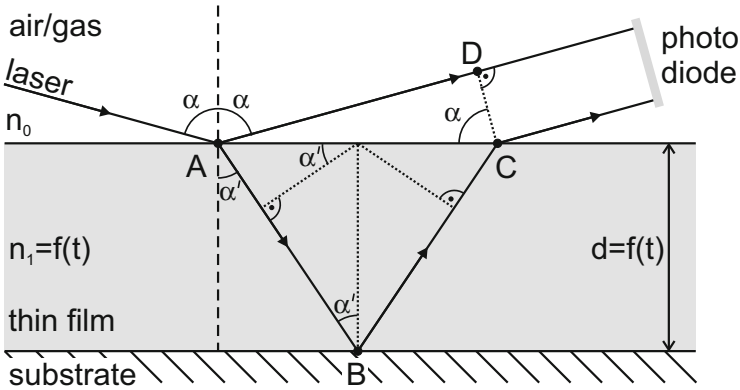

Fig. 2 Optical path of a laser beam through a drying film. The laser light hits and is partly reflected from the film surface with an angle α. At the same time light penetrates into the wet film and experiences a change in direction caused by the higher refractive index n_1 of the solution. The difference in optical path (Δ) of these two beams leads to the appearance of interference

(s = solid, l = liquid) of the components:

$$n_1 = \sum_{i=1}^{K} \varphi_i \cdot n_i, \tag{3}$$

$$\varphi_s = 1 - \varphi_l = d_{\text{dry}}/d, \tag{4}$$

Insertion of Eqs. (2)–(4) into Eq. (1) yields an expression for the calculation of the film thickness:

$$d = \frac{-B + \sqrt{B^2 - 4AC}}{2A}, \tag{5}$$

$$A = n_l^2 - \sin^2\alpha; \;\; B = 2d_{\text{dry}} n_l (n_s - n_l); \;\; C = d_{\text{dry}}^2 (n_s - n_l)^2 - m^2\lambda^2/4,$$

$$x_S = \left(1 + \frac{d_{\text{dry}}}{d - d_{\text{dry}}} \cdot \frac{\rho_s}{\rho_l}\right)^{-1}, \tag{6}$$

The thickness can be converted into mass fractions using Eq. (6), where x_s is the solvent mass fraction and ρ_i are the densities of the liquid and the solid components.

Figure 3 shows the reflectometer signal of a drying P3HT:PCBM in ortho-dichlorobenzene (o-DCB) solution, the associated thickness evolution over time, i.e., the drying curve, and—deduced from the latter—the composition of the solution. The drying process is divided into a constant-rate period, governed by

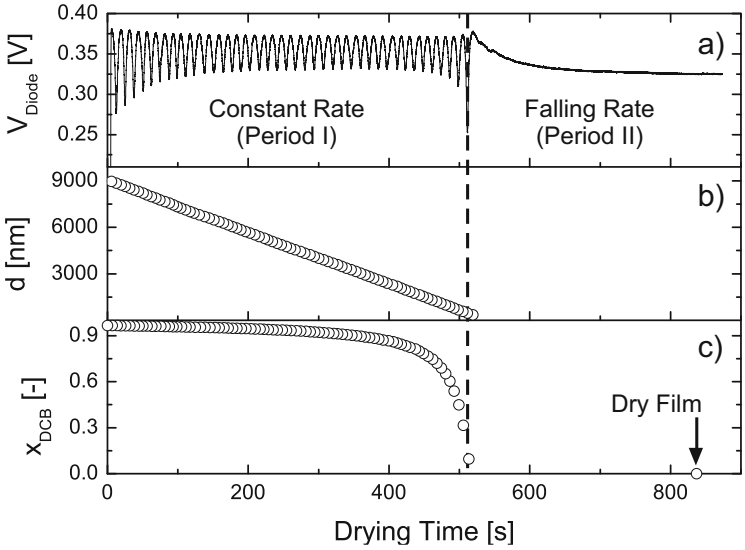

Fig. 3 (**a**) Voltage signal of the reflectometer photodiode. (**b**) Thickness and (**c**) solvent mass fraction evolution over drying time derived from the reflectometer signal. The film is dry when there is no further change of photovoltage [15]

the mass transport of solvent in the gas phase. This phase is characterized by a regular appearance of interference fringes and a linear decrease in film thickness. At low solvent content, the solvent diffusion in the film dominates the drying process and solvent removal is slowed down by orders of magnitudes, defined as the falling rate period. The thickness evolution in this range cannot be resolved, since the thickness change between two interference fringes is about 100 nm for the given setup ($\lambda = 650$ nm, $\alpha = 35°$). The duration of this period can be estimated by the time interval between the last interference fringe and the point where a constant photovoltage is reached. Other methods, such as spectroscopic ellipsometry [16] or quartz crystal microbalances [17, 18], are feasible techniques to resolve changes during this period. In order to predict the drying behavior at given drying parameters, a model for the constant-rate period can be used [12].

2.3 Experimental Details of the GIWAXS Measurements

The real-time GIWAXS studies were performed at beamline ID10B in the European Synchrotron Radiation Facility (ESRF) (Grenoble, France) using the experimental setup shown in Fig. 1. Depending on the experiment, the photon energy varied between 10–12.3 keV. Two-dimensional (2D) diffraction patterns were acquired by an X-ray area detector (MarCCD). The incident angle was set below the critical

angle of the substrate but above the critical angle of the blend. It should be taken into account that the intensity collected with a flat detector in grazing-incidence geometry is not a direct map of reciprocal space and misses a part of the reciprocal space along the vertical direction of the sample [19–21]. Consequently, out-of-plane profiles obtained from the 2D pattern contain an in-plane component of the scattering wave vector transfer (q).

We give values as a function of the magnitude of the scattering vector q determined from the total scattering angle. In our work, complementary measurements with a point detector were performed to obtain specular (along q_z) and in-plane scans (along q_{xy}). The point detector was mounted in a second arm of the diffractometer and was used to align the sample and to collect X-ray reflectivity data before and after each drying experiment. Two-dimensional frames were acquired with an integration time of a few seconds. After each frame, the sample was moved horizontally in the direction of coating by 0.6 mm (the horizontal beam size was controlled by the horizontal slit width, which was 0.5 mm) to measure a fresh region of the film not previously exposed to direct radiation.

As a measure of the crystallinity, the intensity of the (100) was azimuthally integrated, accounting for the orientation distribution of crystallites. The coherence correlation length was measured from the full width at half maximum (FWHM) of the peaks. This is a convolution of the coherence length of the lamellar stacking and crystalline quality.

3 Drying of P3HT/P_{61}CBM

3.1 Binary Phase Diagram and Morphology Development

Before addressing the structure formation of the BHJ in the ternary polymer–fullerene–solvent system (P3HT-PCBM-DCB), we have first determined the phase diagrams of the binary systems P3HT-DCB and PCBM-DCB [7]. Figure 4a depicts the composition of the two coexisting phases of a P3HT solution in DCB for each temperature at thermodynamic equilibrium, namely, the solid-poor sol phase (half-filled circles) and the solid-rich gel phase (filled circles). These two states form the binodal curve which surrounds the thermodynamically unstable two-phase region. If the P3HT solution is situated in this unstable region it tends to phase separate, leading to the aggregation of a swollen polymer with solvent ($x_s = 10.2$ wt% solid fraction) and a residual sol phase (5.1 wt% solid fraction) [22, 23]. The solution is stable at room temperature in the concentration range of 20–40 mg/ml [$x_s = 1.5$–3 wt%; $x_s = m_{\text{solid}}/(m_{\text{DCB}} + m_{\text{solid}})$] usually used for organic solar cells. With solvent evaporation at a constant temperature (the arrow indicates evaporation at 25 °C), the P3HT solution reaches the solubility limit at a solid mass fraction of $x_s = 5.1$ wt% (interpolated for 25 °C) and enters the unstable binodal area. The width of the unstable two-phase region is almost zero at 50 °C (overlapping error

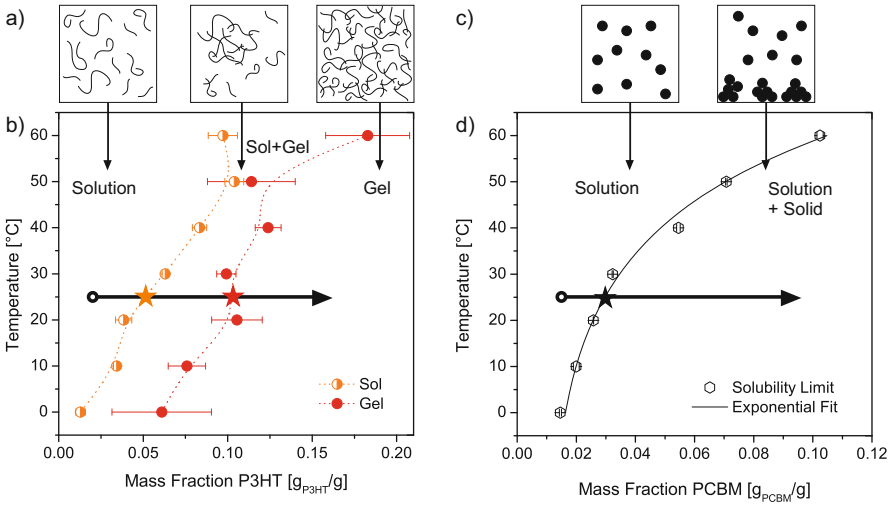

Fig. 4 Binary phase diagram of P3HT and PCBM solutions in dichlorobenzene (DCB). (**a**) Schematic of the transition from solution to gel state with polymer aggregation in the unstable two-phase region, before the solution turns into a higher viscous gel during solvent evaporation. (**b**) Phase diagram of P3HT–DCB solution with unstable two-phase region between the solution and gel state. *Dashed lines* are a visual guide. (**c**) Schematic of fullerene aggregation after crossing the solubility limit. (**d**) Solubility of PCBM in DCB as a function of temperature. The *arrows* indicate the drying process at 25 °C, and the *stars* represent the instant of phase transition [7]

bars), indicating an almost continuous increase of viscosity without phase separation at this drying temperature.

PCBM does not show a gelation behavior and exhibits a single solubility limit, as depicted in Fig. 4d, which increases with temperature, in contrast to P3HT. By crossing the solubility limit caused by solvent evaporation, solid PCBM aggregates precipitate, maintaining the solubility limit as shown schematically in Fig. 4c. Depending on the evaporation kinetics of pure PCBM solution, this can lead to macroscopic crystals of several micrometers [24].

We compared the pathway through the superposition of the binary phase diagrams with the evolution of the crystallization of the ternary blend in thin films, studied in situ using GIWAXS and laser reflectometry. Using the experimental setup explained in Sect. 2, we obtained 2D GIWAXS diffraction patterns immediately after doctor-blading the solution on a glass/poly(3,4-ethylenedioxythiophene) polystyrene sulfonate (PEDOT:PSS) substrate. Figure 5a shows five snapshots of the structural evolution of a P3HT:PCBM (1:0.8) blend during the evaporation of DCB. The solvent mass fraction (x_{DCB}) at each time instant can be obtained from the optical thickness measurement based on interference patterns.

The time evolution of the film composition obtained from laser reflectometry is plotted in Fig. 5b. To study the entire evolution of the solvent fraction, a model of the constant gas-phase mass-transfer coefficient for the film drying kinetics was adapted

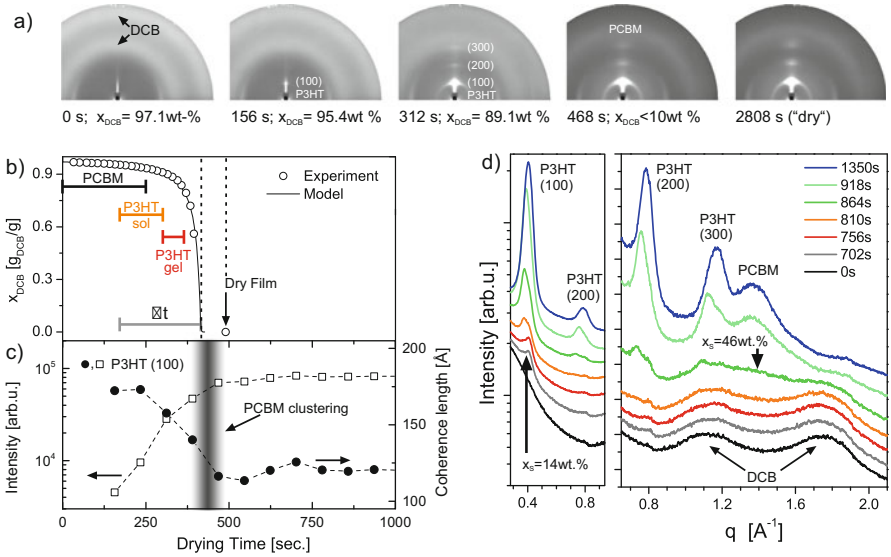

Fig. 5 (**a**) Two-dimensional grazing-incidence wide-angle X-ray spectroscopy diffraction patterns acquired during different stages in the evolution of the film during drying. Below each image, the drying time and actual solvent fraction are mentioned. (**b**) Evolution of film composition (solvent mass fraction x_{DCB}) during film drying (data, symbols; fit from model, line). The labeled bars indicate ranges of phase transitions as expected from the superposition of the binary phase diagrams. The constant-rate period time after crossing P3HT solubility is denoted as Δt. (**c**) The integrated area of the P3HT (100) Bragg peak and the correlation length are plotted vs. drying time. (**d**) Selected profile plots at increasing drying times showing the emergence of the diffraction peaks of PCBM, P3HT (h00) Bragg peaks, and the disappearance of the diffraction peaks of the evaporating solvent (dichlorobenzene) on a silicon dioxide/silicon substrate [7]

to the experimental data [8]. The bars in Fig. 5b labeled PCBM, P3HT (sol), and P3HT (gel) indicate the instants on the timescale when the solubility limits/phase transitions of each component are reached for the binary cases. The length of each bar originates from two cases of transferring the binary phase diagrams to the ternary system as described in detail in [7]. Because of the low solid fraction in highly diluted solutions, the decrease in the solvent mass fraction x_{DCB} proceeds slowly in the beginning. This leads to a long residence time at solvent fractions $x_{DCB} > 85$ wt%. As the solid fraction becomes significant, the solvent fraction x_{DCB} reduces rapidly and a wide range of solvent fractions in the phase diagram is crossed quickly in a small window of drying time, offering little time for further molecular ordering. In the last stage of drying, at high solid fractions $x_{DCB} < 5$ wt%, the evaporation rate decreases because of the limited diffusion of solvent molecules in the film.

We compared the expected ranges of transitions in Fig. 5b, which are proposed according to the binary phase diagrams, with the observed evolution of P3HT crystallinity (Fig. 5c) for the ternary system under investigation. For P3HT, we

initially expect a delay in crystallization until the solubility limit is reached. P3HT nucleation at the solubility limit is expected for a solid mass fraction of $x_s = 5.1$–9.1 wt%, which is confirmed by the appearance of the P3HT (100) lamellar peak in the early stage of film drying ($x_s = 4.6$ wt%). During the constant-rate period the intensity increases; near the range of complete gelation, the second- and third-order Bragg peaks appear. PCBM crystallizes at a later stage of drying.

On PEDOT:PSS-covered substrates it is difficult to decipher the appearance of the PCBM scattering ring ($q = 1.37$ Å^{-1}) following the disappearance of DCB broad diffraction scattering rings (at $q = 1.12$ Å^{-1} and 1.75 Å^{-1}). Hence, a drying experiment was performed without PEDOT:PSS and using a silicon substrate with native silicon oxide because of its low surface roughness. Profile lines at different stages of drying are plotted in Fig. 5d. The drying experiment confirmed the development of the PCBM diffraction ring after crystallization of P3HT at $x_s = 46$ wt%. Even for the highest published PCBM solubility of about 100 mg/ml [24] ($x_s = 7.7$ wt% at room temperature), PCBM would be expected to crystallize at an earlier stage. This shows that polymer crystallization occurs first, followed by PCBM clustering at a later stage of drying. These observations of oppressed PCBM crystallization suggest a strong interaction between fullerene and polymer.

Additional insight in the drying process is obtained from the analysis of the evolution of the (100) lamellar peak with time. The spot-like P3HT (100) Bragg peak ($q \approx 0.4$ A^{-1}) at the earliest stage of drying indicates that the initially formed P3HT nuclei are predominantly oriented with an edge-on configuration. This implies that P3HT nucleation is induced by a planar interface, either at the film–substrate or at the film–air interface. During the solidification there is a progressive shift in the (100) peak position, which indicates a densification of the lamella packing (with a reduction of the spacing from 17.4 to 16.3 Å). The correlation length of the lamellae with the drying time decreases slightly with time (Fig. 5c). The fact that the crystalline correlation length does not increase during the film formation indicates that the crystallization of P3HT occurs as a result of the nucleation of new crystals in the bulk of the wet film rather than as a result of further growth of the initially formed nuclei at the interface. The arcing of the diffracted intensity extending from the (h00) P3HT peaks reveals a rapid increase in the fraction of crystallites tilted with respect to the edge-on orientation during P3HT crystallization. It is worth noting that the decreased correlation length cannot be explained by the decrease in the lamella spacing and suggests an overall smaller lamellar coherence length of P3HT bulk crystallized aggregates than those nucleated at the interface.

The evolution of the blend's structure is schematically illustrated in Fig. 6. Blend solidification proceeds in three steps: (1) the earliest stage of P3HT nucleation at the interface (substrate or air); (2) crystallization of disordered P3HT crystallites out of the wet film; and (3) late formation of PCBM aggregates in the last stage of the drying. We show in Sect. 3.3 that the stage of bulk crystallization is crucial for the development of π–π ordering in P3HT.

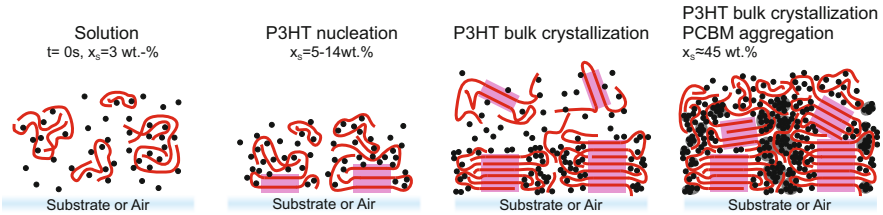

Fig. 6 Scheme of the stages of P3HT:PCBM film formation during solvent (dichlorobenzene) evaporation

In contrast to a low PCBM solubility of only 3–4 % in crystalline P3HT, Collins et al. [25, 26] observed a solubility of about 16 % in amorphous P3HT regions. This confirms the image of three coexisting phases: (1) mainly pure crystalline P3HT domains comprising very few PCBM inclusions; (2) an intermixed phase formed by amorphous P3HT regions containing higher amounts of PCBM molecules; and (3) PCBM-rich clusters partly intermixed in the amorphous P3HT regions. PCBM-solving additives may selectively reduce the interaction between P3HT and PCBM and promote polymer crystallization; this strategy has been used to improve the PCE with the use of mixed solvents and additives [1, 26–28].

3.2 Effect of the Blend Ratio

Previous works have reported that the optimum P3HT:PCBM weight ratio composition for the best device performance is close to 1:0.8 [29–35]. To understand the role of PCBM in the crystallization of P3HT during film drying, we investigated the structural evolution for P3HT:PCBM blends in weight ratios of 1:0.5, 1:0.8, and 1:2 on glass/PEDOT:PSS [10]. Figure 7c displays four 2D X-ray scattering frames illustrating different stages of drying for each of the investigated blend weight ratios. The appearance of the P3HT (100), (200), and (300) is indicated in the drying paths of the phase diagram of different blending ratios (Fig. 7a). The structural evolution with drying time observed for the blends with ratios 1:0.5 and 1:0.8 is similar and matches the picture of film formation illustrated in Fig. 6: an initial interface nucleation of edge-on P3HT crystallites followed by P3HT bulk crystallization, with a consequent increase in the orientation distribution, and late aggregation of PCBM. The evolution is remarkably different for the blend with a 1:2 ratio, that is, with a larger amount of PCBM. First, the appearance of the P3HT (100) Bragg peak ($x_{DCB} = 92$ wt%) is delayed [as were the development of the (200) and (300) peaks], which can be attributed to the increased intermixing of P3HT and PCBM because of the larger amount of PCBM. Another striking difference is that for the blend with a 1:2 ratio, the (h00) peaks maintain a spot-like shape during drying, that

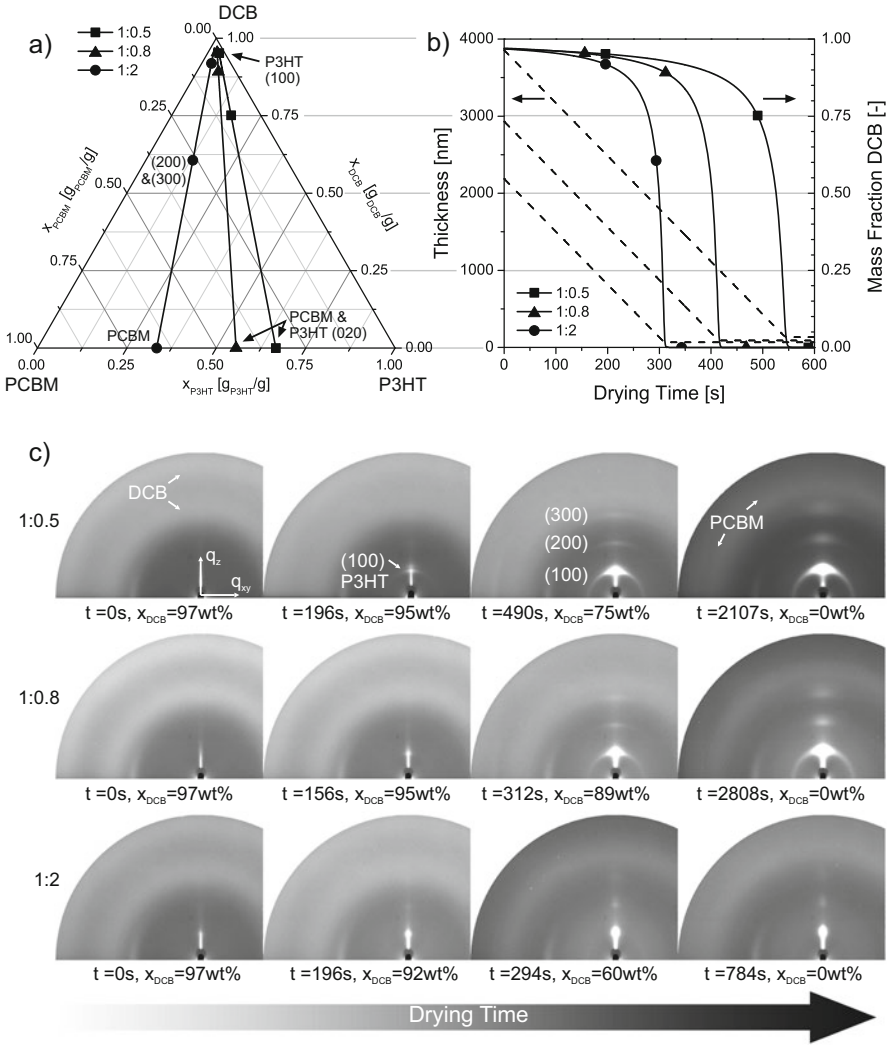

Fig. 7 (**a**) Drying path through the phase diagram of different P3HT:PCBM blending ratios at 25 °C. *Symbols* indicate the appearance of P3HT (100) Bragg peak, (200) and (300), and the PCBM diffraction ring in order of appearance from *top* to *bottom*. (**b**) Drying kinetics of the investigated films. Each symbol represents a grazing-incidence X-ray diffraction measurement. *Filled symbols* are related to the instants of structural changes indicated in the ternary phase diagram. (**c**) Two-dimensional X-ray diffraction patterns at different instants of evaporation of the solvent (dichlorobenzene) for three blend ratios [36]

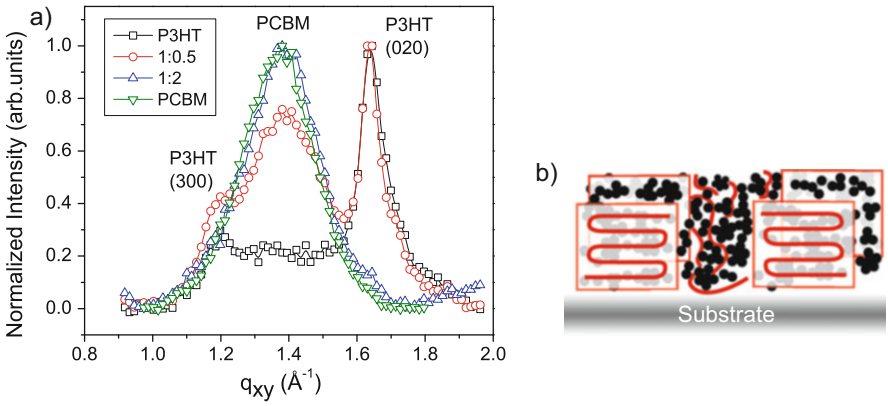

Fig. 8 (**a**) In-plane data using a point detector of films consisting of pure P3HT (*black squares*), P3HT:PCBM blend with 1:0.5 ratio (*red circles*), P3HT:PCBM blend with 1:2 ratio (*blue triangles*), and pure PCBM (*green inverted triangles*). (**b**) Schematic picture of the disruption of π–π stacking of P3HT polymer chains by PCBM [10]

is, lamellae with an edge-on orientation. In spite of the lamella organization with an edge-on orientation, in-plane GIWAXS data scans reveal that the π–π stacking of the polymer backbones is suppressed by PCBM: The scans lack the characteristic in-plane (020) peak ($q = 1.64$ Å) [37] that is observed for films of pure P3HT and for blends with ratios of 1:0.5 and 1:1.8 (Fig. 8). This observation is confirmed by optical absorption spectra data [10].

Our results confirm that increased loading of PCBM in the solution significantly inhibits the P3HT ordering during the bulk crystallization stage. Interface-induced nucleation of edge-on crystallites with lamellar ordering seems not to be hindered although the intermixing of P3HT and PCBM at a molecular level hinders the π–π stacking of P3HT polymer chains. This is an important issue because the π–π ordering is considered beneficial for the delocalization and mobility of charge carriers and polaron excitations over neighboring chains. An alternative explanation recently proposed by Richter et al. [28] attributes the suppression of the crystallization of P3HT by PCBM to polymer vitrification caused by the increased glass transition temperature (T_g) of the mixed amorphous phase formed by P3HT and PCBM.

3.3 *Effect of the Drying Temperature*

As we already mentioned, the structural development during drying can be influenced with solvent mixtures or with additives. The substrate temperature is another parameter that can be used to influence the nanomorphology formation during drying. The drying temperature influences several parameters, including the solubility

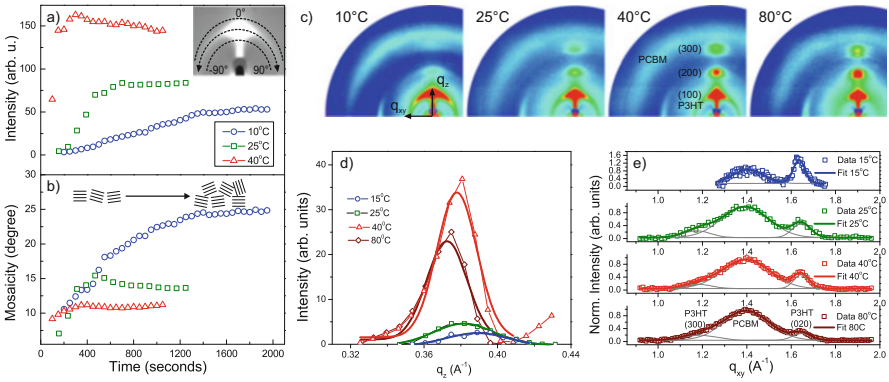

Fig. 9 Evolution with drying time of (**a**) P3HT (100) integrated intensity and (**b**) orientation distribution (mosaicity) for drying at substrate temperatures of 10, 25, and 40 °C. (**c**) Two-dimensional diffraction pattern measured for the dried P3HT:PCBM films upon drying at the indicated temperatures. (**d**) X-ray specular data with Gaussian fits (*thick continuous line*) of P3HT (100) Bragg peak for films dried at different substrate temperatures (15–80 °C). (**e**) Grazing-incidence X–ray diffraction data with Gaussian fits of the same dried films (normalized to maximum) [9]

and the diffusion kinetics in gas and liquid phases. To study the structural evolution during drying, we doctor-bladed a 1:0.8 solution of P3HT and PCBM dissolved in DCB on PEDOT:PSS-coated glass substrates at substrate temperatures of 10, 25, 40, and 80 °C. The thickness decreased as the processing temperature increased because of the lower viscosity of the wet film for a constant solid fraction. The solid fraction of the blend–solvent film was kept constant in order to start the drying process at the same position in the phase diagram.

The evolution with drying time of the overall integrated (100) intensity and of the orientation distribution is depicted in Fig. 9a and b, respectively. The drying proceeds faster at higher temperatures. In the earliest stage of P3HT nucleation, a similar orientation distribution is observed at all substrate temperatures. During film drying at lower temperatures, a larger fraction of misaligned crystallites develops than at higher-temperature drying. The larger orientation distribution of P3HT crystallites for the films dried at lower temperatures can be related to the slower kinetics of film formation. Similar observations were reported for solvent annealed spin-coated films in comparison with faster drying [33, 38]. Nevertheless the results reveal better (100) crystallinity for the films dried at higher temperatures (and with faster drying), that is, a larger fraction of aggregates with lamellar stacking. Drying at higher temperatures also leads to better alignment of the polymer chains with an edge-on orientation. The 2D diffraction patterns obtained for dried films are shown in Fig. 9c.

Further quantitative structural information on the ordering perpendicular and parallel to the substrate surface was obtained by a point detector. X-ray specular and in-plane data are plotted in Fig. 9d and e, respectively. The higher specular

X-ray intensity of the (100) Bragg peak for P3HT:PCBM blends dried at higher drying temperatures confirms better lamellar packing. The mean coherence length of the P3HT (100) peak increases with the drying temperature from 194 Å at 15 °C to 308 Å at 80 °C. It is difficult to hypothesize any major effect on devices from differences in lamellae organization since this direction of the crystalline structure is less relevant for charge generation or transport. Of higher relevance is the π–π organization of the polymer. In-plane GIWAXS data in Fig. 9e show the P3HT (020) in-plane peak, demonstrating the π–π assembly of P3HT chains for all four drying temperatures. We note, however, that the π–π crystallinity increases significantly with lower drying temperatures, as revealed by the larger intensity of the P3HT (020) peak. Additionally, the coherence length of the π–π stacking within the P3HT layers was largest for the sample dried at the lowest temperature: 118 Å at a drying temperature of 15 °C vs. 77 Å at 80 °C. Increased π–π ordering for the films dried at lower temperatures has been corroborated by the optical absorption spectra. The morphology of the films measured by atomic force microscopy upon PCBM removal reveals that the size of PCBM clusters increase as the drying temperature increases, most likely as a result of the stronger increase in PCBM solubility at higher temperatures [7].

These results suggest that the drying time after the solubility limit (Δt) is crossed, that is, during P3HT bulk crystallization, is crucial for π–π ordering (see Fig. 5b). Drying at a higher temperature leads to a larger lamellar organization; however, the higher solvent evaporation rate reduces the time that interchain P3HT π–π stacking can develop.

We measured how the solar cell efficiency is affected by drying at different temperatures; Fig. 10 summarizes the results. Further information can be found in [7]. We performed experiments with two drying gas velocities with two different nitrogen flow rates for each of the drying temperatures. The time after crossing solubility (Δt) decreased for higher-temperature drying. The short-circuit current density and PCE (Fig. 10b) are plotted as a function of Δt in Fig. 10. The solar cell efficiency increased with lower-temperature—and thus slower—drying, according to the longer crystallization time after crossing the P3HT solubility. This trend still existed after postannealing the samples for 5 min at 150 °C.

In terms of high-throughput fabrication, a long drying process is not desirable. Our in situ crystallization studies of film drying have shown that the initial drying period prior to crossing the P3HT solubility does not contribute to the polymer crystallization. One strategy to decrease the overall drying time is altering the thermodynamics of phase separation by adding an "unfriendly" solvent for both components, reducing the solubility of P3HT and PCBM [39]. For instance, if one adds the "unfriendly" solvent cyclohexanone (CHN) to chlorobenzene (CB) solution of P3HT:PCBM, the solubility can be crossed prior to the drying process. We performed a real-time GIWAXS study of P3HT:PCBM from a solvent mixture of CHN:CB (1:1) and demonstrated the formation of a P3HT (100) diffraction ring directly after coating ($t = 0$), confirming the crystallization of randomly oriented

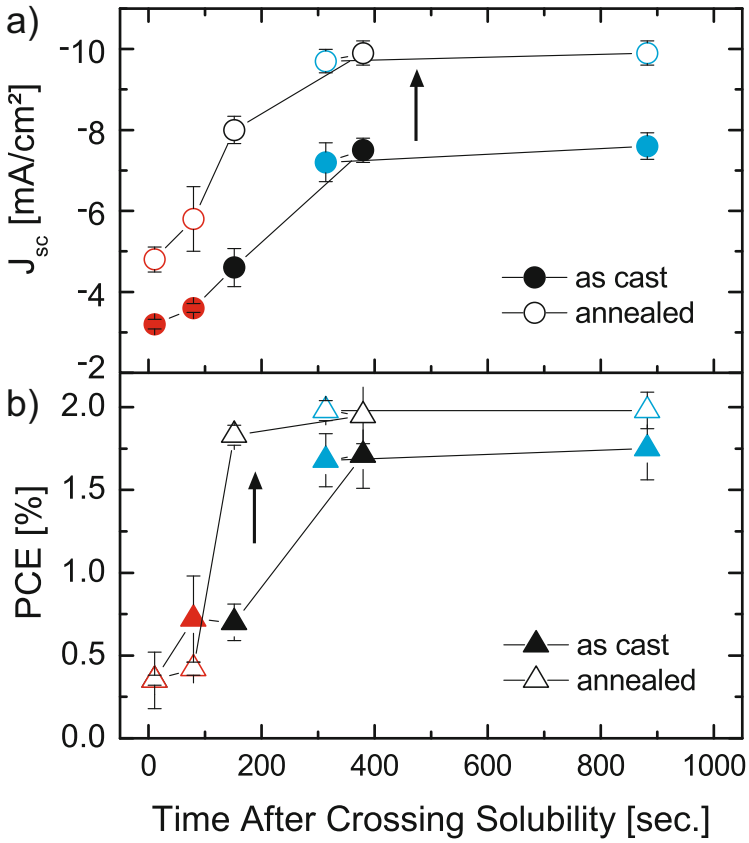

Fig. 10 (**a**) Short-circuit current density and (**b**) power conversion efficiency of the untreated (*filled symbols*) and for 5 min at 150 °C annealed (*open symbols*) solar cells plotted against the drying time after crossing P3HT solubility for films dried at 15, 25, 40 °C drying temperatures at a nitrogen flow of 0.15 and 0.5 m/s [7]

solid-like P3HT aggregates in the dispersion and, therefore, the acceleration of polymer aggregation [7].

4 Drying of PSBTBT:$PC_{71}BM$

The PCE of P3HT:PCBM solar cells is limited to maximum values of approximately 4–5 % [40]. This limit can be overcome by introducing low-bandgap polymers that are able to absorb light also at higher wavelengths above 600 nm and therefore cover a higher fraction of the solar spectrum [41]. The use of the asymmetric fullerene derivative $PC_{71}BM$ further promotes the efficiency because of an increased

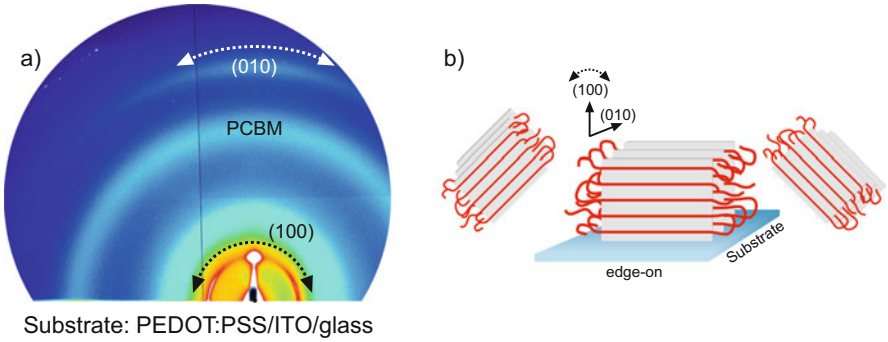

Fig. 11 (**a**) Grazing-incidence X-ray diffraction pattern of PSBTBT:$PC_{71}BM$ cast from dichlorobenzene. (**b**) Schematic representation of the edge-on configuration of PSBTBT crystallites [36]

absorption in the visible region compared to PCBM. For PSBTBT, one of the earlier synthesized low-bandgap polymers for photovoltaics, PCEs of 5.5 % have been reported at a blending ratio of 1:2 PSBTBT:$PC_{71}BM$ in single devices [42–46]. The polymer is characterized by a neutral-color absorption in the visible spectrum, making it an ideal candidate for the manufacturing of semitransparent solar cells [47]. In tandem devices, which comprise two active layers harvesting sunlight in complementary regions of the solar spectrum, efficiencies of 5.8 % have been reported with the use of PSBTBT [48, 49]. This concept was expanded to ternary blends consisting of two photoactive polymers and a fullerene component. Consequently, the interplay between processing and morphology in these blends is even more complex [50–52].

Figure 11 depicts a 2D GIWAXS diffraction pattern of PSBTBT:$PC_{71}BM$ cast from o-DCB showing the diffraction features commonly observed for this system: the (010) diffraction scattering ring attributed to the π–π stacking, the (100) peak indicative of the lamellar organization, and the prominent broad diffraction scattering ring from amorphous $PC_{71}BM$. In contrast to P3HT, blends with PSBTBT exhibit a broader orientation distribution, being beneficial for charge transport into all directions of the photoactive layer. This chapter highlights similarities of the P3HT:PCBM and PSBSBT:$PC_{71}BM$ systems, as we try to present a more generalized description of the drying process of photovoltaic polymer:fullerene blends.

4.1 In situ Study of the Crystallization of PSBTBT:$PC_{71}BM$

The structural evolution during drying in o-DCB has been investigated for PSBTBT:$PC_{71}BM$ with the reportedly optimal weight ratio of 1:2. As in the preparation of a P3HT:PCBM casting solution, PSBTBT:$PC_{71}BM$ is dissolved

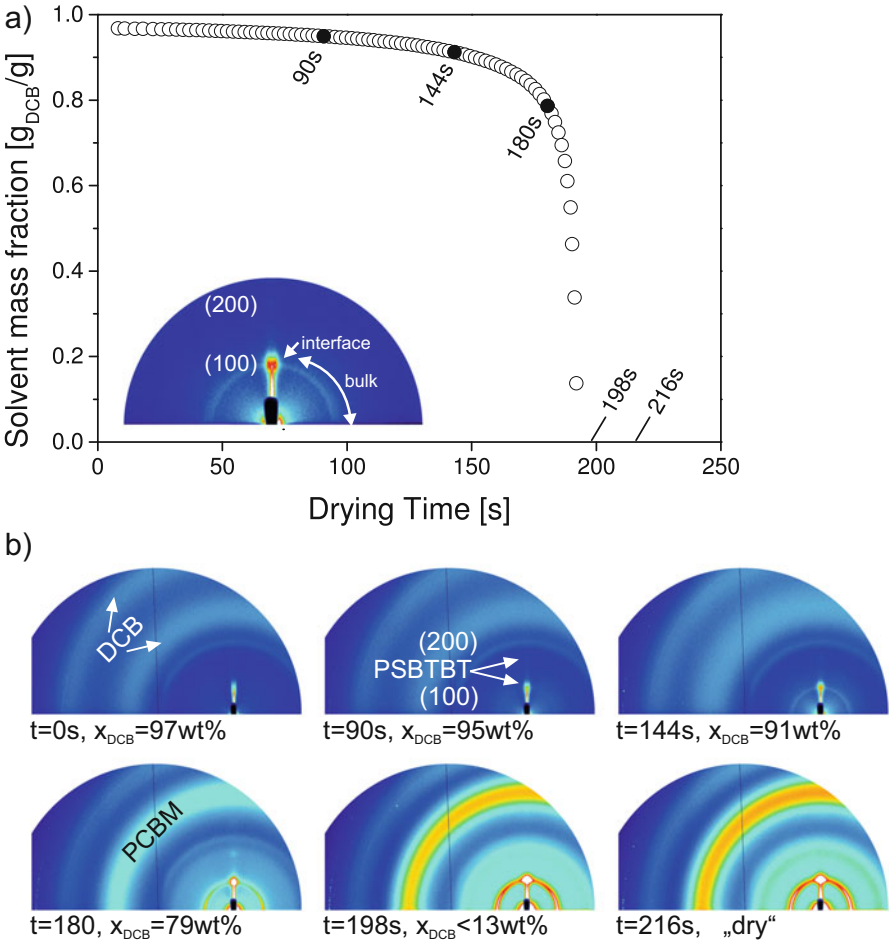

Fig. 12 Evolution of (**a**) solvent mass fraction and (**b**) grazing-incidence X-ray diffraction (GIXD) patterns during the drying of PSBTBT:$PC_{71}BM$ (1:2) film cast from dichlorobenzene at 40 °C. The *filled symbols* in the drying curve and the stated time correspond to the GIXD images [36]

at a low solid content (PSBTBT:$PC_{71}BM$:DCB = 1:2:97 wt%). This leads to comparable drying kinetics during the initial constant-rate period, where only the properties of the solvent govern the drying process. Similarly, the drying kinetics are characterized by a long residence time at a high solvent mass fraction with a steep decrease at the end toward a low solvent content, as depicted in Fig. 12a. After this decrease the solution enters the falling-rate period, where the diffusional mass transport is the dominating mechanism.

Figure 12b summarizes the structural evolution of the drying blend. At $X_{DCB} = 95$ wt% the onset of (100) polymer aggregation is observed. The spot-like shape of the (100) peak indicates that crystallites lie parallel to the

substrate surface with an edge-on orientation. As for P3HT:PCBM, this suggests the onset of nucleation in the vicinity of an interface, either the substrate or the surface of the drying solution. In contrast to P3HT:PCBM, this material system shows the concomitant appearance of a sharp powder-like diffraction ring with (100) spacing after 108 s, indicating that a significant portion of the polymer component crystallizes under a random orientation (see caption in Fig. 12a). Thus, different from P3HT, during the initial constant-rate period of drying, PSBTBT also crystallizes in the bulk solution, giving evidence of strong intermolecular interactions between PSBTBT molecules as reported in previous studies [46]. During the drying, the (100) crystallinity increases (from both the bulk and the interface). The crystallization rate significantly increases after 180 s ($X_{DCB} \approx 79$ wt%), when the strong $PC_{71}BM$ diffraction signals appear, indicating the aggregation of $PC_{71}BM$ [36]. This suggests a certain molecular miscibility of $PC_{71}BM$ with PSBTBT, as $PC_{71}BM$ is expected to aggregate earlier [53]. A (010) diffraction ring also emerges, revealing π–π-stacked aggregates of PSBTBT randomly oriented in the film. Figure 13 summarizes the crystallization process.

4.2 *Effect of the Drying Temperature*

A broad orientation distribution of polymer crystallites and the development of π–π stacking turned out to be beneficial for photoactive layers consisting of P3HT:PCBM. For PSBTBT the π–π stacking is visible by the appearance of a (010) ring (Fig. 12) and a pronounced absorption shoulder at 760 nm in the optical absorption spectrum (Fig. 14b). Studying the effect of the drying temperature on the film formation [36] has shown that the drying temperature does not significantly influence either the crystallinity or the orientation distribution of PSBTBT. The independence from the casting temperature is visible in the absorption spectra

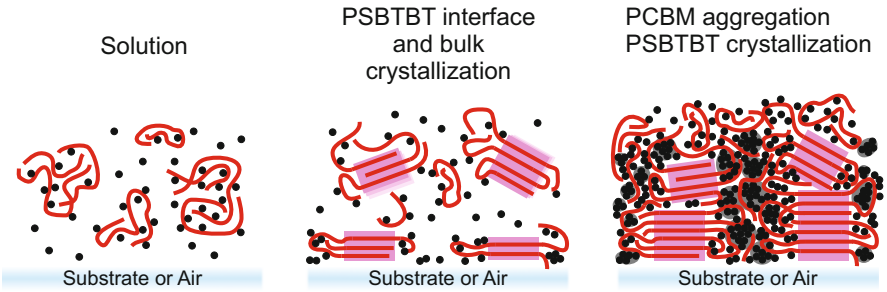

Fig. 13 Schematic of the drying process for PSBTBT:$PC_{71}BM$. Unlike P3HT, there is coexisting nucleation of PSBTBT in solution and at the interface ($X_{DCB} \approx 95$ wt%), followed by a stage of $PC_{71}BM$ aggregation ($X_{DCB} \approx 80$ wt%) and rapid crystallization of PSBTBT

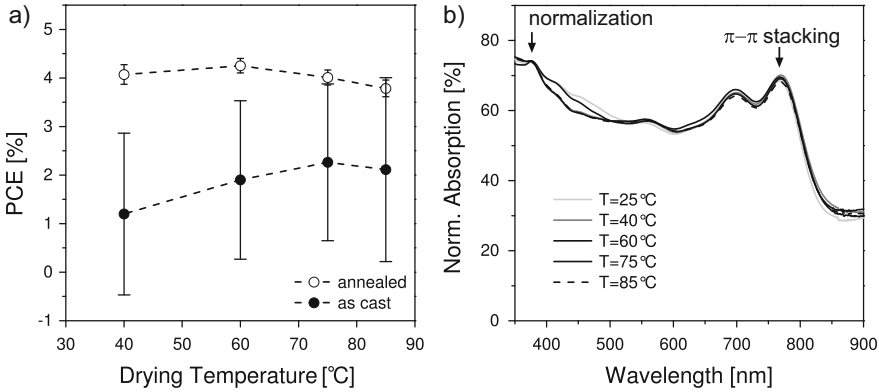

Fig. 14 Effect of the drying temperature and annealing on PSBTBT:$PC_{71}BM$ (**a**) device performance and (**b**) absorption spectra. The latter are normalized to the $PC_{71}BM$ absorption peak at 375 nm [36]

(Fig. 14a). Similarly, postannealing treatment does not cause appreciable changes in the film structure [36].

The comparison of PCEs of as-cast and annealed solar cells is shown in Fig. 13a for different drying temperatures ranging from 40–85 °C. The PCE of the as-casted films is not significantly affected by the drying temperature. There is a large dispersion in the PCE value obtained for OPV devices before annealing, which is mainly caused by interface effects; these are reduced after thermal treatment.

As a consequence, PSBTBT:$PC_{71}BM$ proves to be a photoactive blend whose film formation is largely independent of the drying kinetics or processing conditions. This is attributed to the early polymer aggregation in solution, plausibly giving rise to a rapid π–π assembly. The relative insensitivity of the nanomorphology formation to the drying conditions is possibly a result of the strong interaction of PSBTBT molecules in solution as proposed earlier by Chen et al. [45]. This enables manufacturing of cells at a constant efficiency, even for inhomogeneous drying conditions, making PSBTBT:$PC_{71}BM$ a good material for the large-scale production of 4.5–5 % PCE solar cells [2, 5, 25, 28, 29].

5 Conclusions

We have shown that real-time studies of the film formation during drying by combined laser reflectometry and GIWAXS provide fundamental knowledge of how the components may self-organize at different stages in the ternary phase diagram (i.e., the solvent, donor material, and acceptor material). Furthermore, the influencing parameters or kinetic factors for controlled film morphology during drying can be identified to improve the solar cell performance.

In this review we have shown that the structure formations for P3HT:PCBM and PSBTBT:$PC_{71}BM$ are remarkably different. For P3HT:PCBM blends, P3HT crystallization starts at the interface and is followed by crystallization in the bulk of the wet film and by the late aggregation of PCBM in the final stage of drying. We identify the intermediate stage of bulk crystallization during drying to be particularly significant with regard to the π–π self-organization of the polymer. We have found evidence of strong polymer–fullerene interactions that impede the crystal growth of PCBM and disrupt the π–π stacking of P3HT. Sufficiently slow drying of P3HT–PCBM at low temperatures allows the polymer molecules to assemble and reach a favorable nanomorphology driven by the slow organization of P3HT in solution and the spatially limited aggregation of $P_{61}CBM$. For PSBTBT, the predominant mechanism for BHJ nanoscale morphology seems to be crystallization of the polymer, which takes place in the bulk of the solution from the earliest stage. There is coexisting nucleation of PSBTBT in solution and at the interface, followed by a stage of $PC_{71}BM$ aggregation ($X_{DCB} \approx 80$ wt%) and rapid crystallization of PSBTBT. The final nanomorphology of PSBTBT:$PC_{71}BM$ is not significantly influenced by drying conditions such as temperature and drying gas velocity. Since short drying times are not detrimental for the optoelectronic device properties of PSBTBT, these materials should be advantageous for fast production speeds.

Although the number of in situ studies represents a small percentage of the overall literature about the characterization of BHJs, the importance of gaining an understanding of the dynamics of crystallization can be recognized in the increasing number of in situ studies published in recent years [16, 28, 53–62]. It is expected that a combination of complementary techniques capable of gaining insight into the nanomorphology formation at different length- and timescales will offer a better understanding of the nature of the different phases formed (a mixture of polymer-rich, fullerene-rich, and mixed polymer–fullerene domains) and their implications for charge transport and charge generation. Moreover, dynamic studies are of general applicability to a wide range of solution-processed materials and systems beyond OPV research.

6 Acknowledgments

We thank the German Research Foundation (DFG) for funding our project within the Priority Program 1355, “Elementary Processes of Organic Photovoltaics” (BA 3772/1-1, RU 342/25-2, BA 3772/1-2, BA 3772/1-3). We acknowledge the European Synchrotron Radiation Facility (ESRF) for providing synchrotron radiation facilities and Alexei Vorobiev and Oleg Konovalov for their support. We thank Ralf Weigel for his support in the MPI–MF beamline of the Synchrotron Radiation Facility ANKA (Karlsruhe). We thank all the coworkers involved in this project, in particular, Prof. Dr. Helmut Dosch, Dr. Erik Ahlswede, Prof. Dr. Sigurd Höger, Dr.

Alexander Colsmann, Dr. Felix Pasker, Dr. Jonas Hanisch, Dr. Andreas Bauer, Dr. Aina Quintilla, and Dr. Carmen Munuera.

References

1. Liao H-C et al (2013) Additives for morphology control in high-efficiency organic solar cells. Mater Today 16(9):326–336
2. Liu F et al (2013) Characterization of the morphology of solution-processed bulk heterojunction organic photovoltaics. Prog Polym Sci 38(12):1990–2052
3. Treat ND, Chabinyc ML (2014) Phase separation in bulk heterojunctions of semiconducting polymers and fullerenes for photovoltaics. Annu Rev Phys Chem 65:59–81
4. Clarke TM et al (2008) Free energy control of charge photogeneration in polythiophene/fullerene solar cells: the influence of thermal annealing on P3HT/PCBM blends. Adv Funct Mater 18(24):4029–4035
5. Chen F-C et al (2010) Morphological study of P3HT:PCBM blend films prepared through solvent annealing for solar cell applications. Sol Energy Mater Sol Cells 94(12):2426–2430
6. Liu X et al (2012) Solvent additive control of morphology and crystallization in semiconducting polymer blends. Adv Mater 24(5):669–674
7. Schmidt-Hansberg B et al (2011) Moving through the phase diagram: morphology formation in solution cast polymer-fullerene-blend films for organic solar cells. ACS Nano 5(11):8579–8590
8. Schmidt-Hansberg B et al (2009) In situ monitoring the drying kinetics of knife coated polymer-fullerene films for organic solar cells. J Appl Phys 106(12):124501
9. Sanyal M et al (2011) In situ X-ray study of drying-temperature influence on the structural evolution of bulk-heterojunction polymer-fullerene solar cells processed by doctor-blading. Adv Energy Mater 1(3):363–367
10. Sanyal M et al (2011) Effect of photovoltaic polymer/fullerene blend composition ratio on microstructure evolution during film solidification investigated in real time by X-ray diffraction. Macromolecules 44(10):3795–3800
11. Schmidt-Hansberg B et al (2012) Investigation of non-halogenated solvent mixtures for high throughput fabrication of polymer–fullerene solar cells. Sol Energy Mater Sol Cells 96:195–201
12. Schmidt-Hansberg B et al (2011) Spatially resolved drying kinetics of multi-component solution cast films for organic electronics. Chem Eng Process Process Intensif 50(5–6):509–515
13. Bergqvist J et al (2013) In situ reflectance imaging of organic thin film formation from solution deposition. Sol Energy Mater Sol Cells 114:89–98
14. Heriot SY, Jones RA (2005) An interfacial instability in a transient wetting layer leads to lateral phase separation in thin spin-cast polymer-blend films. Nat Mater 4(10):782–786
15. Schmidt-Hansberg B (2012) Process-structure-property relationship of polymer-fullerene bulk heterojunction films for organic solar cells: drying process, film structure and optoelectronic properties. Cuvillier, Göttingen
16. Wang T et al (2010) The development of nanoscale morphology in polymer:fullerene photovoltaic blends during solvent casting. Soft Matter 6(17):4128–4134
17. Vogt BD et al (2005) Moisture absorption into ultrathin hydrophilic polymer films on different substrate surfaces. Polymer 46(5):1635–1642
18. Eastman SA et al (2012) Effect of confinement on structure, water solubility, and water transport in Nafion thin films. Macromolecules 45(19):7920–7930
19. Baker JL et al (2010) Quantification of thin film crystallographic orientation using X-ray diffraction with an area detector. Langmuir 26(11):9146–9151

20. Muller-Buschbaum P (2014) The active layer morphology of organic solar cells probed with grazing incidence scattering techniques. Adv Mater 26(46):7692–7709
21. Rivnay J et al (2012) Quantitative determination of organic semiconductor microstructure from the molecular to device scale. Chem Rev 112(10):5488–5519
22. van Krevelen DW (1990) Properties of polymers: their correlation with chemical structure: their numerical estimation and prediction from additive group contributions. Elsevier, Amsterdam
23. Yang X et al (2004) Crystalline organization of a methanofullerene as used for plastic solar-cell applications. Adv Mater 16(9–10):802–806
24. Yao Y et al (2008) Effects of solvent mixtures on the nanoscale phase separation in polymer solar cells. Adv Funct Mater 18(12):1783–1789
25. Westacott P et al (2013) On the role of intermixed phases in organic photovoltaic blends. Energy Environ Sci 6(9):2756
26. Collins BA, Tumbleston JR, Ade H (2011) Miscibility, crystallinity, and phase development in P3HT/PCBM solar cells: toward an enlightened understanding of device morphology and stability. J Phys Chem Lett 2(24):3135–3145
27. DeLongchamp DM et al (2011) Molecular characterization of organic electronic films. Adv Mater 23(3):319–337
28. Richter LJ et al (2015) In situ morphology studies of the mechanism for solution additive effects on the formation of bulk heterojunction films. Adv Energy Mater 5(3):1400975
29. Dennler G, Scharber MC, Brabec CJ (2009) Polymer-fullerene bulk-heterojunction solar cells. Adv Mater 21(13):1323–1338
30. Ma W et al (2005) Thermally stable, efficient polymer solar cells with nanoscale control of the interpenetrating network morphology. Adv Funct Mater 15(10):1617–1622
31. Li G et al (2005) High-efficiency solution processable polymer photovoltaic cells by self-organization of polymer blends. Nat Mater 4(11):864–868
32. Mihailetchi VD et al (2006) Origin of the enhanced performance in poly(3-hexylthiophene): [6,6]-phenyl C61-butyric acid methyl ester solar cells upon slow drying of the active layer. Appl Phys Lett 89(1):012107
33. Li G et al (2007) "Solvent annealing" effect in polymer solar cells based on poly(3-hexylthiophene) and methanofullerenes. Adv Funct Mater 17(10):1636–1644
34. Shin M et al (2010) Abrupt morphology change upon thermal annealing in poly(3-hexylthiophene)/soluble fullerene blend films for polymer solar cells. Adv Funct Mater 20(5):748–754
35. Campoy-Quiles M et al (2008) Morphology evolution via self-organization and lateral and vertical diffusion in polymer:fullerene solar cell blends. Nat Mater 7(2):158–164
36. Schmidt-Hansberg B et al (2012) Structure formation in low-bandgap polymer:fullerene solar cell blends in the course of solvent evaporation. Macromolecules 45(19):7948–7955
37. Brinkmann M et al. (2014) Understanding the structure and crystallization of regioregular poly (3-hexylthiophene) from the perspective of epitaxy, vol 265. Springer, Heidelberg, pp 83–106
38. Chu C-W et al (2008) Control of the nanoscale crystallinity and phase separation in polymer solar cells. Appl Phys Lett 92(10):103306
39. Moulé AJ, Meerholz K (2008) Controlling morphology in polymer–fullerene mixtures. Adv Mater 20(2):240–245
40. Dang MT, Hirsch L, Wantz G (2011) P3HT:PCBM, best seller in polymer photovoltaic research. Adv Mater 23(31):3579–3602
41. Bundgaard E, Krebs FC (2007) Low band gap polymers for organic photovoltaics. Sol Energy Mater Sol Cells 91(11):954–985
42. Scharber MC et al (2010) Influence of the bridging atom on the performance of a low-bandgap bulk heterojunction solar cell. Adv Mater 22(3):367–370
43. Maurano A et al (2010) Recombination dynamics as a key determinant of open circuit voltage in organic bulk heterojunction solar cells: a comparison of four different donor polymers. Adv Mater 22(44):4987–4992

44. Hou J et al (2008) Synthesis, characterization, and photovoltaic properties of a low band gap polymer based on silole-containing polythiophenes and 2,1,3-benzothiadiazole. J Am Chem Soc 130(48):16144–16145
45. Chen HY et al (2010) Silicon atom substitution enhances interchain packing in a thiophene-based polymer system. Adv Mater 22(3):371–375
46. Morana M et al (2010) Nanomorphology and charge generation in bulk heterojunctions based on low-bandgap dithiophene polymers with different bridging atoms. Adv Funct Mater 20(7):1180–1188
47. Colsmann A et al (2011) Efficient semi-transparent organic solar cells with good transparency color perception and rendering properties. Adv Energy Mater 1(4):599–603
48. Chou C-H et al (2011) A metal-oxide interconnection layer for polymer tandem solar cells with an inverted architecture. Adv Mater 23(10):1282–1286
49. Sista S et al (2010) Highly efficient tandem polymer photovoltaic cells. Adv Mater 22(3):380–383
50. Ameri T et al (2013) Organic ternary solar cells: a review. Adv Mater 25(31):4245–4266
51. Koppe M et al (2010) Near IR sensitization of organic bulk heterojunction solar cells: towards optimization of the spectral response of organic solar cells. Adv Funct Mater 20(2):338–346
52. Ameri T et al (2012) Performance enhancement of the P3HT/PCBM solar cells through NIR sensitization using a small-bandgap polymer. Adv Energy Mater 2(10):1198–1202
53. Pearson AJ et al (2014) Morphology development in amorphous polymer:fullerene photovoltaic blend films during solution casting. Adv Funct Mater 24(5):659–667
54. Agostinelli T et al (2011) The role of alkane dithiols in controlling polymer crystallization in small band gap polymer:fullerene solar cells. J Polym Sci B 49(10):717–724
55. Rogers JT et al (2011) Structural order in bulk heterojunction films prepared with solvent additives. Adv Mater 23(20):2284–2288
56. Rogers JT et al (2012) Time-resolved structural evolution of additive-processed bulk heterojunction solar cells. J Am Chem Soc 134(6):2884–2887
57. Pearson AJ, Wang T, Lidzey DG (2013) The role of dynamic measurements in correlating structure with optoelectronic properties in polymer:fullerene bulk-heterojunction solar cells. Rep Prog Phys 76(2):022501
58. Engmann S et al (2015) Real-time X-ray scattering studies of film evolution in high performing small-molecule-fullerene organic solar cells. J Mater Chem A 3(16):8764–8771
59. Chou KW et al (2013) Spin-cast bulk heterojunction solar cells: a dynamical investigation. Adv Mater 25(13):1923–1929
60. Schmidt K et al (2014) A mechanistic understanding of processing additive-induced efficiency enhancement in bulk heterojunction organic solar cells. Adv Mater 26(2):300–305
61. Smilgies D-M et al (2013) Look fast: crystallization of conjugated molecules during solution shearing probed in-situ and in real time by X-ray scattering. Phys Status Solidi RRL 7(3):177–179
62. Wei Chou K et al (2014) Late stage crystallization and healing during spin-coating enhance carrier transport in small-molecule organic semiconductors. J Mater Chem C 2(28):5681–5689